

## Article

# NiO-MgO Prepared by the Complex-Decomposition Method as a Catalyst for Carbon Dioxide Reforming of Methane

Ying Wang, Bin Li, Yong-Shan Xiao and Zhong-Wen Liu \* 

Key Laboratory of Syngas Conversion of Shaanxi Province, School of Chemistry and Chemical Engineering, Shaanxi Normal University, Xi'an 710119, China

\* Correspondence: zwliu@snnu.edu.cn

**Abstract:** The NiO-MgO solid solution has been proven to be an efficient catalyst for the carbon dioxide reforming of methane (CRM). However, the challenge is still there for the facilely controlled synthesis of the single-phase solid solution with the uniform composition, and the interactions between NiO and MgO are not consistently correlated with the CRM performance. To address these issues, in this work, the complex-decomposition method was applied to regulate the chemical and structural properties of NiO-MgO catalysts via simply changing the complexing agent, calcination temperature, and Ni/Mg molar ratio. The catalysts were comparatively evaluated for CRM under severe reaction conditions of 750 °C, 0.1 MPa, CH<sub>4</sub>/CO<sub>2</sub> = 1, and a gas hourly space velocity of 60000 mL·g<sup>-1</sup>·h<sup>-1</sup>. Irrespective of the complexing agents investigated, NiO-MgO solid solution was exclusively formed. However, the structural and reductive properties of the NiO-MgO catalysts were strongly dependent on the complexing agent, which is reasonably explained as the varied coordinative capabilities of the complexing agent with the metal cations. Moreover, the highest CRM performance, i.e., the initial CH<sub>4</sub> conversion of ~86% kept constant for a time-on-stream of 20 h, was achieved over the Ni<sub>0.1</sub>Mg<sub>0.9</sub>O catalyst by using glycine as the complexing agent and calcined at 800 °C. The characterization and CRM results vigorously confirmed that a good balance between the sintering and the in situ release of active metallic Ni under CRM reaction conditions was constructed over the NiO-MgO catalyst prepared using glycine as the complexing agent, leading to its highest stability. Considering the simple procedure of the complex-decomposition method and the convenient adjustment of the NiO and MgO interactions by simply changing the complexing agent and calcination temperature, the thus developed catalyst can be applied for extensive understanding the CRM mechanism, and extended for large-scale preparation.

**Keywords:** carbon dioxide; methane; syngas; NiO-MgO; complex-decomposition



**Citation:** Wang, Y.; Li, B.; Xiao, Y.-S.; Liu, Z.-W. NiO-MgO Prepared by the Complex-Decomposition Method as a Catalyst for Carbon Dioxide Reforming of Methane. *Processes* **2023**, *11*, 596. <https://doi.org/10.3390/pr11020596>

Academic Editors: Shetian Liu, Zhen Zhao and Mingsheng Luo

Received: 30 December 2022

Revised: 7 February 2023

Accepted: 14 February 2023

Published: 16 February 2023



**Copyright:** © 2023 by the authors. Licensee MDPI, Basel, Switzerland. This article is an open access article distributed under the terms and conditions of the Creative Commons Attribution (CC BY) license (<https://creativecommons.org/licenses/by/4.0/>).

## 1. Introduction

The catalytic carbon dioxide reforming of methane (CRM) has been established as a promising process to efficiently convert the potent greenhouse gases of CO<sub>2</sub> and CH<sub>4</sub> to the value-added synthesis gas with a stoichiometric H<sub>2</sub>/CO ratio of 1 [1,2], which satisfies the synthesis of chemicals [3,4], such as methanol [5] and dimethyl ether [6]. Moreover, CRM also opens an alternative way for the direct utilization of natural gas (mainly composed of CH<sub>4</sub>) with a high CO<sub>2</sub> level, such as marine gas [7,8]. In this context, CRM has attracted much attention in the academic and industrial domains. Unfortunately, due to the high partial pressure of CO and high reaction temperature, the commercialization of the CRM process is still bottlenecked by catalyst deactivation, which is mainly induced by the coke deposition and sintering of metal catalysts [9,10].

Generally, nickel is regarded as an applicable catalyst for industrial CRM owing to its relatively higher activity, lower cost, and reasonable availability compared to noble metals [11,12]. To improve long-term stability, abundant studies have focused on Ni-based catalysts with improved capacities of anti-coking and anti-sintering. Therefore, different

strategies are practiced to achieve this target. Among the currently available methods, adding basic oxides such as  $\text{La}_2\text{O}_3$  [13] to adjust the acid-base properties of the support has been reported to be an effective route in inhibiting the coke deposition, which is commonly explained as the enhanced chemisorption of  $\text{CO}_2$  by the basic center over the Ni-based catalysts [14]. Alternatively, the partial neutralization of the Lewis acid sites with the added basic oxides is also conducive to alleviated coke deposition [15,16].

In the case of the Ni metal, its interaction with support is regulated as a general strategy to optimize the dispersion and reduction extent of Ni, which has been proven to be an important factor in determining the performance of Ni-based catalysts for CRM. As the lower limit, the isolated Ni atoms over Ce-doped hydroxyapatite are reported to be intrinsically coke resistant due to the limited deep decomposition of methane into carbon [17]. In contrast, comparative results over the single-atom  $\text{Ni}_1/\text{Mg}(100)$  and single-site  $\text{Ni}_4/\text{Mg}(100)$  catalysts indicate that the formation of the confined single-site Ni/MgO is required for catalyzing CRM over NiO-MgO solid solutions [18]. Different from these observations, single-crystalline MgO and the synergetic effect between Ni and Mo bimetals are essential for the coke- and sintering-resistant NiMo CRM catalysts [19]. Thus, considering the pioneering work of the Ni-MgO solid solution as an efficient CRM catalyst [20], the effects of the interactions between Ni and MgO in the solid solution on the CRM performance are still worthy of investigation. Theoretically, the formation of Ni-MgO solid solution with continuously varied Ni contents is possible [21]. However, the synthesis of NiO-MgO solid solution with well-defined crystals free of segregated phases such as NiO is still an issue provided that the slightly varied radii of  $\text{Ni}^{2+}$  (69 pm) and  $\text{Mg}^{2+}$  (78 pm) cations are taken into account. Thus, the controlled preparation of solid solutions with varied Ni and MgO interactions is beneficial not only to the development of a high-performance CRM catalyst, but also to the better understanding of the CRM mechanism. In this context, we found that the complex-decomposition method is effective in regulating the interactions between Ni and  $\text{SiO}_2$  via simply changing the complexing agent [22].

Based on these understandings, in this work, the complex-decomposition method was applied to prepare a series of NiO-MgO catalysts with different compositions. Importantly, the simple changing of the complexing agent with varied molecular structures and coordinative groups proved to be effective in regulating the interactions between NiO and MgO, leading to significant effects on the catalytic performance of Ni-MgO for CRM. Among the complexing agent studied, the  $\text{Ni}_{0.1}\text{Mg}_{0.9}\text{O}$  catalyst, by using glycine as the complexing agent, showed the best CRM performance.

## 2. Experimental Section

### 2.1. Catalysts Preparation

The NiO-MgO solid solutions were prepared via the complex-decomposition method by using nickel acetate tetrahydrate ( $\text{Ni}(\text{CH}_3\text{COO})_2 \cdot 4\text{H}_2\text{O}$ ) and magnesium acetate tetrahydrate ( $\text{Mg}(\text{CH}_3\text{COO})_2 \cdot 4\text{H}_2\text{O}$ ) as the metal precursors. Glacial acetic acid (Gla), oxalic acid (Oxa), urea, and amino acids including glycine (Gly), proline (Pro), serine (Ser), and alanine (Ala), were used as the complexing agent and fuel, respectively. The typical procedure is reported in our previous work [22]. Specifically, predetermined amounts of nickel acetate tetrahydrate and magnesium acetate tetrahydrate were dissolved in 40 mL of ethanol under stirring. By keeping the molar ratio of the complexing agent to the total amounts of the precursors of nickel and magnesium at 1, the desired amount of complexing agent was dissolved in 40 mL of deionized water. To carry out the complex-decomposition process, the two solutions were mixed, and subsequently stirred at 60 °C until a gel was formed. After burning the gel in the air, the obtained solid was calcined for 6 h with a heating rate of 2 °C·min<sup>-1</sup>. According to the calcination temperature and composition, the prepared catalysts were labeled as  $\text{Ni}_x\text{Mg}_{1-x}\text{O-T-Y}$ , where x, T, Y represent the Ni loading, calcination temperature, and complexing agent used, respectively.

## 2.2. Catalysts Characterization

The phase compositions of fresh, reduced, and spent catalysts were obtained from powder X-ray diffraction (XRD) on a D8 Advance X-ray diffractometer (Bruker) over a scattering angle ( $2\theta$ ) from  $10^\circ$  to  $90^\circ$  at a step of  $0.02^\circ$  with the acquisition time of 0.2 s. In the case of the reduced catalysts, the reduction was performed at  $700^\circ\text{C}$  for 2 h under a flow of  $50\text{ mL}\cdot\text{min}^{-1}$   $\text{H}_2/\text{N}_2$  with a molar ratio of 2/3. After cooling to room temperature, the sample was directly transferred for XRD analysis.

The textural properties of fresh catalysts were determined by the  $\text{N}_2$ -physisorption method over a BelSorp-Max surface area and porosity analyzer (BEL), which was operated at  $-196^\circ\text{C}$ .

TEM images of reduced and spent catalysts were obtained on a FEI Tecnai G2 F20 microscope (FEI). The particle size distribution was determined by counting 200 particles.

The reduction behavior of the fresh catalysts was analyzed by means of the  $\text{H}_2$  temperature-programmed reduction ( $\text{H}_2$ -TPR), which was carried out on a Autochem 2020 chemisorption analyzer (Micromeritics). Before  $\text{H}_2$ -TPR, a 50 mg sample was heated to  $500^\circ\text{C}$  in a pure Ar flow of  $30\text{ mL}\cdot\text{min}^{-1}$  to eliminate the adsorbed water and impurities. After cooling down to  $50^\circ\text{C}$ ,  $10\%\text{H}_2/\text{Ar}$  flow ( $30\text{ mL}\cdot\text{min}^{-1}$ ) was switched and the temperature was heated to  $1000^\circ\text{C}$  with a temperature ramp of  $10^\circ\text{C}\cdot\text{min}^{-1}$ . The  $\text{H}_2$  consumption was monitored by a thermal conductivity detector (TCD).

The amount of coke formed on spent catalysts was measured via thermogravimetric differential scanning calorimetry (TG-DSC) on a STA449 F5 thermogravimetric analyzer (Netzsch). To perform the TG-DSC test, 5 mg of the spent catalyst was loaded, and the temperature was increased from  $25$  to  $900^\circ\text{C}$  at a temperature ramp of  $10^\circ\text{C}\cdot\text{min}^{-1}$  in an air flow.

## 2.3. CRM Reaction

The CRM experiment was conducted on a vertical quartz fixed-bed reactor (OD: 11 mm, ID: 8 mm) by loading 100 mg of each catalyst (40–60 mesh) diluted with 1.0 g of quartz sands (40–60 mesh). Prior to the catalytic test, the in situ reduction of the catalyst in a flow of  $50\text{ mL}\cdot\text{min}^{-1}$   $\text{H}_2/\text{N}_2$  ( $\text{H}_2/\text{N}_2 = 2/3$ ) was performed at  $700^\circ\text{C}$  for 2 h. After this, a pure  $\text{N}_2$  flow was switched, and kept for 30 min. By increasing the temperature to  $750^\circ\text{C}$ , the dilution-free reactants with a  $\text{CH}_4/\text{CO}_2$  molar ratio of 1 were introduced for starting the CRM reaction. For all of the tests, the reaction conditions were kept the same, i.e., 0.1 MPa,  $750^\circ\text{C}$ , and gas hourly space velocity (GHSV) of  $60,000\text{ mL}\cdot\text{g}^{-1}\cdot\text{h}^{-1}$ . After condensing water in an ice-cold trap, the effluent was online separated and analyzed by GC-9560 gas chromatography (Shanghai Huaai Chromatographic Analysis Co., Ltd., Shanghai, China) equipped with Molecular Sieve 5A and Porapak Q capillary columns. The detailed analysis conditions and the calculations are given in our previous work [14,22], and the equations for calculating the conversions of  $\text{CH}_4$  ( $C_{\text{CH}_4}$ ),  $\text{CO}_2$  ( $C_{\text{CO}_2}$ ), and the  $\text{H}_2/\text{CO}$  molar ratio in the products ( $R_{\text{H}_2/\text{CO}}$ ) are given as follows.

$$C_{\text{CH}_4} (\%) = (F_{\text{CH}_4, \text{inlet}} - F_{\text{CH}_4, \text{outlet}}) / F_{\text{CH}_4, \text{inlet}} \times 100\%$$

$$C_{\text{CO}_2} (\%) = (F_{\text{CO}_2, \text{inlet}} - F_{\text{CO}_2, \text{outlet}}) / F_{\text{CO}_2, \text{inlet}} \times 100\%$$

$$R_{\text{H}_2/\text{CO}} = F_{\text{H}_2, \text{outlet}} / F_{\text{CO}, \text{outlet}}$$

where  $F$  stands for the flow rate.

## 3. Results and Discussion

### 3.1. Effects of Complexing Agents

The impact of complexing agents on the phase compositions was investigated by XRD (Figure 1). Irrespective of the complexing agent used, all of the fresh catalysts exhibited almost the same XRD patterns with obvious diffractions at  $2\theta$  of  $37^\circ$ ,  $43^\circ$ ,  $63^\circ$ ,  $75^\circ$ , and  $79^\circ$  (Figure 1A). These diffractions are assigned to  $\text{MgO}$  (JCPDS 87-0653) or  $\text{MgO}$ -based

NiO-MgO solid solutions [23]. Due to the slight difference between the radii of the  $\text{Ni}^{2+}$  (69 pm) and  $\text{Mg}^{2+}$  (78 pm) cations, it is well known that the XRD peaks of MgO are shifted to a higher diffraction angle if NiO-MgO solid solution is formed [24]. This is more clearly illustrated by enlarging the XRD peak at about  $43^\circ$  as a representative (the right side of Figure 1A); i.e., a  $0.6^\circ$  shift from  $43.1$  to  $43.7^\circ$  depends on the complexing agent used. Thus, the NiO-MgO solid solution is formed for all of the catalysts, the amount of which is affected by the complexing agent. This observation can be explained by the structure, molecular size, and coordinative groups of the complexing agent. When the structures of various complexing agents were carefully examined, a smaller steric hindrance was apparent for glycine, glacial acetic acid, oxalic acid, and urea compared to that for proline, serine, and alanine, which favors coordination with  $\text{Ni}^{2+}$  cations. Although NiO-MgO solid solution was formed over all of the catalysts, the extent was promoted when the complex agent with a smaller steric hindrance was used. If the molecular nature of the complexing agents was taken into account, glycine, oxalic acid, and urea possessed more complexing groups ( $-\text{COOH}$ ,  $-\text{NH}_2$ ), which are expected to supply a higher coordinative capacity. Consequently, the formation of the solid solution was favored, which was reflected by the relatively obvious shift to a higher angle compared to that of  $\text{Ni}_{0.1}\text{Mg}_{0.9}\text{O}-800\text{-Gla}$ . Moreover, the maximum shifts were observed for  $\text{Ni}_{0.1}\text{Mg}_{0.9}\text{O}-800\text{-Gly}$  and  $\text{Ni}_{0.1}\text{Mg}_{0.9}\text{O}-800\text{-Urea}$  due to the  $-\text{COOH}$  group possessing a higher coordinative ability with  $\text{Ni}^{2+}$  cations than that of  $-\text{NH}_2$ . As a result of the larger steric hindrance, the coordination of proline and alanine with  $\text{Ni}^{2+}$  becomes difficult, leading to more obvious free NiO species over  $\text{Ni}_{0.1}\text{Mg}_{0.9}\text{O}-800\text{-Pro}$  and  $\text{Ni}_{0.1}\text{Mg}_{0.9}\text{O}-800\text{-Ala}$ , as revealed from the relatively remarkable NiO diffraction. In contrast, no obvious NiO species were formed on  $\text{Ni}_{0.1}\text{Mg}_{0.9}\text{O}-800\text{-Ser}$ , although the serine molecules also showed greater steric hindrance, which could reasonably be attributed to the additional coordination of  $-\text{OH}$  groups with  $\text{Ni}^{2+}$ .

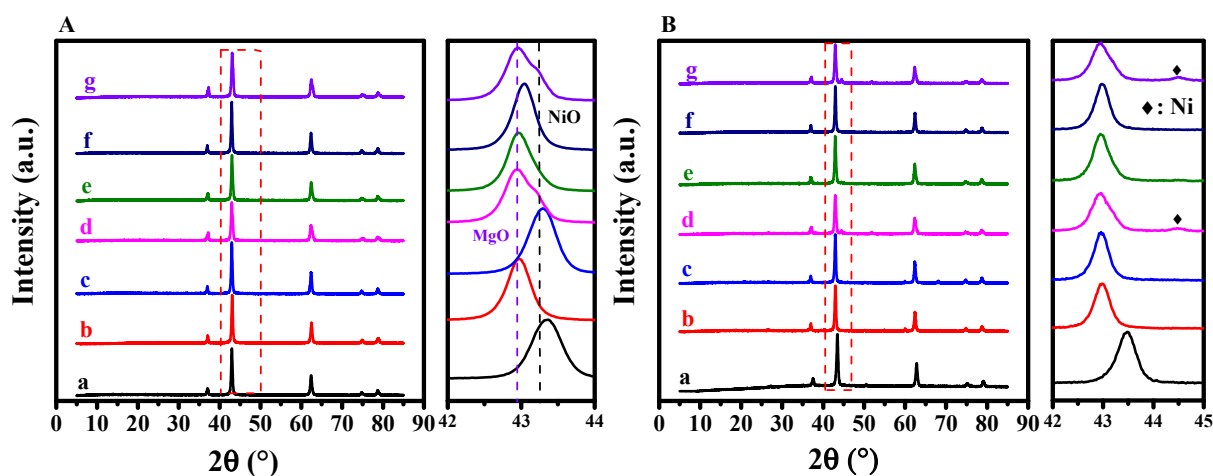


**Figure 1.** XRD patterns of the fresh (A) and reduced (B) catalysts of  $\text{Ni}_{0.1}\text{Mg}_{0.9}\text{O}-800\text{-Gly}$  (a),  $\text{Ni}_{0.1}\text{Mg}_{0.9}\text{O}-800\text{-Gla}$  (b),  $\text{Ni}_{0.1}\text{Mg}_{0.9}\text{O}-800\text{-Oxa}$  (c),  $\text{Ni}_{0.1}\text{Mg}_{0.9}\text{O}-800\text{-Pro}$  (d),  $\text{Ni}_{0.1}\text{Mg}_{0.9}\text{O}-800\text{-Ser}$  (e),  $\text{Ni}_{0.1}\text{Mg}_{0.9}\text{O}-800\text{-Urea}$  (f),  $\text{Ni}_{0.1}\text{Mg}_{0.9}\text{O}-800\text{-Ala}$  (g).

The XRD patterns of reduced catalysts are shown in Figure 1B. Apparently, the characteristic diffractions of NiO-MgO solid solution were still maintained. Apart from these diffractions, an obvious diffraction of metallic Ni at about  $44.5^\circ$  was observed for  $\text{Ni}_{0.1}\text{Mg}_{0.9}\text{O}-800\text{-Pro}$  and  $\text{Ni}_{0.1}\text{Mg}_{0.9}\text{O}-800\text{-Ala}$ . This clearly indicates the presence of large-sized Ni crystalline grains, which probably originate from the reduction of the segregated NiO phase; i.e., free NiO particles. In contrast, the XRD diffraction of metallic Ni was absent for the remaining catalysts. These results clearly confirm that the coordinative capacity of the complexing agent with  $\text{Ni}^{2+}$  is critical for the formation of NiO-MgO solid solution, the reduction of which leads to smaller Ni particles. This will be further discussed together with the TEM observations.

The textural information of the fresh catalysts was obtained from N<sub>2</sub>-physisorption results (Figure S1). All of the samples displayed the type IV isotherm with different hysteresis loops. Specifically, a H2 hysteresis loop was shown for Ni<sub>0.1</sub>Mg<sub>0.9</sub>O-800-Gly, Ni<sub>0.1</sub>Mg<sub>0.9</sub>O-800-Ser, and Ni<sub>0.1</sub>Mg<sub>0.9</sub>O-Oxa, and an H3 hysteresis loop was observed for the remaining samples, characterizing the mesoporous structure and heterogeneous pore networks, respectively. These observations can be ascribed as the structure-directing or templating effect of the complexing agent via the coordination with metal cations [25]. As a result of the varied effects induced by the molecular structure of the complexing agents, different surface areas, pore volumes, and average pore sizes are shown for all of the catalysts (Table 1). Moreover, variations in the textural parameters are generally consistent with the changing order for the molecular sizes of the complexing agent, which has been reported in our previous work on the synthesis of Ni-SiO<sub>2</sub> catalysts by the complex-decomposition method [22]. However, the changes for all of the textural parameters, i.e., the BET surface area, pore volume, and average pore size, were not very significant, irrespective of the complexing agent used (Table 1). Moreover, the correlation between the textural properties and the molecular size of the complexing agent is not very strong. If the sintering effect induced from the high-temperature calcination is considered, this may reasonably be ascribed to the diminished textural parameters since the samples were calcined at 800 °C. Thus, as a result of the molecule-size effect of the complexing agent and high-temperature calcination, the textural parameters of the catalysts are slightly varied.

**Table 1.** Textural properties of the fresh Ni<sub>0.1</sub>Mg<sub>0.9</sub>O catalysts prepared with different complexing agents.

Catalysts	BET Surface Area (m <sup>2</sup> ·g <sup>-1</sup> )	Pore Volume (cm <sup>3</sup> ·g <sup>-1</sup> )	Average Pore Size (nm)
Ni <sub>0.1</sub> Mg <sub>0.9</sub> O-800-Gly	25.5	0.15	23.3
Ni <sub>0.1</sub> Mg <sub>0.9</sub> O-800-Gla	27.4	0.13	21.2
Ni <sub>0.1</sub> Mg <sub>0.9</sub> O-800-Oxa	34.6	0.39	35.1
Ni <sub>0.1</sub> Mg <sub>0.9</sub> O-800-Pro	26.0	0.31	20.5
Ni <sub>0.1</sub> Mg <sub>0.9</sub> O-800-Ser	34.5	0.24	34.1
Ni <sub>0.1</sub> Mg <sub>0.9</sub> O-800-Urea	27.7	0.17	21.3
Ni <sub>0.1</sub> Mg <sub>0.9</sub> O-800-Ala	28.1	0.24	34.5

TEM images of the reduced catalysts showed that the Ni nanoparticles with varied sizes were randomly distributed in the bulk MgO (Figure S2). Specifically, relatively larger Ni particles were predominant on Ni<sub>0.1</sub>Mg<sub>0.9</sub>O-800-Pro and Ni<sub>0.1</sub>Mg<sub>0.9</sub>O-800-Ala, as confirmed by the Ni particle size distribution centered at 3.0–5.0 nm. In contrast, the majority of Ni particles over the remaining catalysts were concentrated in the range of 1.5–5.0 nm. As a result, the average particle sizes for Ni<sub>0.1</sub>Mg<sub>0.9</sub>O-800-Pro and Ni<sub>0.1</sub>Mg<sub>0.9</sub>O-800-Ala were 4.1 ± 0.3 nm and 4.2 ± 0.3 nm, which were slightly larger than those of the remaining samples (3.2–3.5 nm). The slightly larger average sizes of metallic Ni over the reduced Ni<sub>0.1</sub>Mg<sub>0.9</sub>O-800-Pro and Ni<sub>0.1</sub>Mg<sub>0.9</sub>O-800-Ala catalysts can be reasonably ascribed as the larger steric hindrance of proline and alanine, which inhibits the effective complexing with Ni<sup>2+</sup> cations. As a result of the smaller steric hindrance and/or higher amounts of coordinative groups, very similarly smaller Ni particles were obtained over the remaining catalysts. Thus, the Ni particle sizes over all of the catalysts are essentially affected by the coordinative capacities of the complexing agents induced by either the coordinative groups and/or the steric hindrance of the molecule.

The reduction behaviors were analyzed by H<sub>2</sub>-TPR (Figure 2). The H<sub>2</sub>-TPR profiles included several H<sub>2</sub>-consumption peaks, and three regions were assigned from the peak temperatures. According to previous classifications [26], the peak below 500 °C is due to the reduction of the weakly bound NiO species, and the 500–800 °C peak is usually associated with the reduction of Ni<sup>2+</sup> ions in the outermost layer and sub-surface layers of the MgO lattice. Moreover, the appearance of the very high-temperature peak (>800 °C) is commonly attributed to the reduction in Ni<sup>2+</sup> ions in the MgO matrix. Apparently, only a trace of weakly bound NiO species existed on Ni<sub>0.1</sub>Mg<sub>0.9</sub>O-800-Urea and Ni<sub>0.1</sub>Mg<sub>0.9</sub>O-800-Ser, as

revealed by the very low  $H_2$  consumption peak at about 460 and 470 °C, respectively. This is consistent with the fact that no corresponding diffractions were detected by XRD (Figure 1A). In the cases of  $Ni_{0.1}Mg_{0.9}O$ -800-Pro and  $Ni_{0.1}Mg_{0.9}O$ -800-Ala, the peaks with considerable  $H_2$  consumption were observed in the range of 500–800 °C. As indicated from the XRD results (Figure 1A), free NiO species were clearly detected for the fresh  $Ni_{0.1}Mg_{0.9}O$ -800-Pro and  $Ni_{0.1}Mg_{0.9}O$ -800-Ala catalysts. Thus, it is reasonable to assign the  $H_2$  consumption to the reduction of the NiO species strongly bound with MgO, which is different from the reference classification [26]. For the remaining samples, the assignment of the  $H_2$  consumption at 500–800 °C was still valid since the diffractions of NiO species were also not detected by XRD. If the peak areas of the  $H_2$  consumptions are taken into account, the amounts of the free NiO species were clearly varied over these catalysts synthesized by using different complexing agents. By examining the reduction peak above 800 °C, the peak temperature varied from about 850 to ~910 °C, which can be attributed to the reduction of NiO having different interactions with MgO in the NiO-MgO solid solution. Specifically, this is confirmed by the much higher peak temperature of 900 °C for  $Ni_{0.1}Mg_{0.9}O$ -800-Gly having stronger interactions between NiO and MgO in the solid solution than those for  $Ni_{0.1}Mg_{0.9}O$ -800-Gla and  $Ni_{0.1}Mg_{0.9}O$ -800-Oxa (850 °C). The phenomena are reasonably associated with the diffusion of  $Ni^{2+}$  into the MgO lattice, which is determined by the structure, molecular size, and coordinative groups of the complexing agent. Thus, these results vigorously prove that both the free NiO species and the interactions between NiO and MgO in the solid solution can be facily adjusted in relatively wide ranges by simply changing the complexing agent.

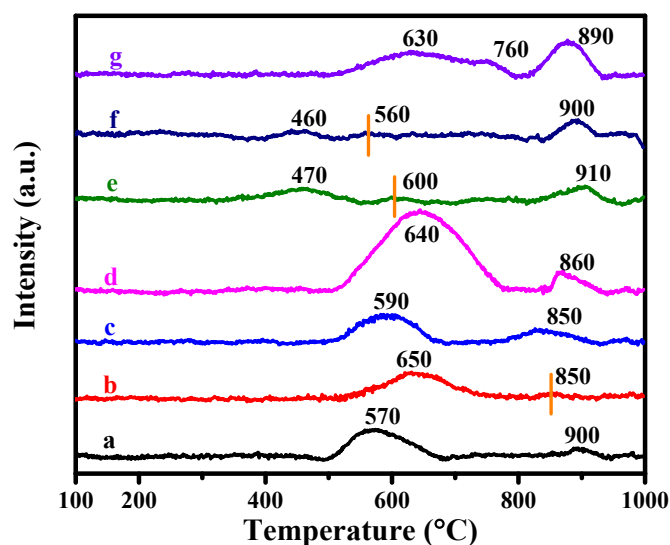


**Figure 2.**  $H_2$ -TPR profiles for the as-prepared catalysts of  $Ni_{0.1}Mg_{0.9}O$ -800-Gly (a),  $Ni_{0.1}Mg_{0.9}O$ -800-Gla (b),  $Ni_{0.1}Mg_{0.9}O$ -800-Oxa (c),  $Ni_{0.1}Mg_{0.9}O$ -800-Pro (d),  $Ni_{0.1}Mg_{0.9}O$ -800-Ser (e),  $Ni_{0.1}Mg_{0.9}O$ -800-Urea (f),  $Ni_{0.1}Mg_{0.9}O$ -800-Ala (g).

### 3.2. CRM Performance

The time-on-stream (TOS) results of CRM are shown in Figure 3. As revealed from Figure 3A,B,  $CO_2$  conversions were higher than  $CH_4$  conversions, irrespective of the catalysts evaluated. This clearly indicates the occurrence of the reverse water-gas shift reaction (RWGS). As a result, the  $H_2/CO$  molar ratios were achieved in the range of 0.9–0.95 (Figure 3C). Moreover, all of the catalysts exhibited a high initial  $CH_4$  conversion of around 80–86% (Figure 3A), indicating the high catalytic activity of the materials for CRM. In the cases of  $Ni_{0.1}Mg_{0.9}O$ -800-Pro and  $Ni_{0.1}Mg_{0.9}O$ -800-Ala, the  $CH_4$  conversions encountered a gradual decrease at a TOS of 10 h and then stayed constant. Moreover,  $Ni_{0.1}Mg_{0.9}O$ -800-Ser showed a continuously slight decrease in  $CH_4$  conversion after a TOS of about 5 h. For the remaining catalysts, the  $CH_4$  conversions were kept almost constant until the end of the

test. Thus, the optimal CRM performance was achieved over  $\text{Ni}_{0.1}\text{Mg}_{0.9}\text{O}$ -800-Gly if both the methane conversion and stability of the catalyst were taken into account.

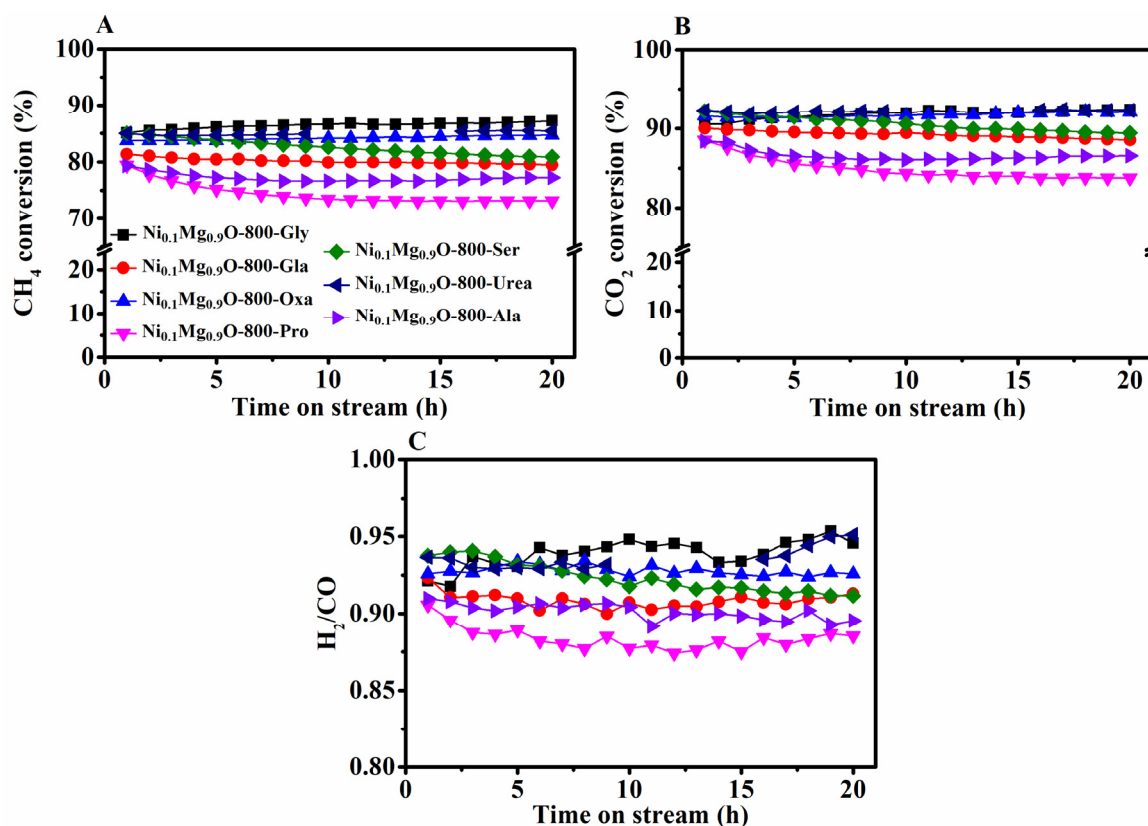


**Figure 3.** The time-on-stream conversions of  $\text{CH}_4$  (A) and  $\text{CO}_2$  (B), and the  $\text{H}_2/\text{CO}$  molar ratio (C) in the products for  $\text{Ni}_{0.1}\text{Mg}_{0.9}\text{O}$  catalyzed CRM under the conditions of  $\text{CH}_4/\text{CO}_2 = 1$ ,  $750^\circ\text{C}$ ,  $0.1\text{ MPa}$  and GHSV of  $60,000\text{ mL}\cdot\text{g}^{-1}\cdot\text{h}^{-1}$ .

### 3.3. Characteristics of the Spent Catalysts

In order to verify the anti-sintering and anti-coking capacities, the spent catalysts were analyzed by XRD, TG-DSC, and TEM in detail.

From the XRD patterns of the spent catalysts (Figure 4A), clear differences were found in comparison with those of the reduced counterparts (Figure 1B). For all of the spent catalysts, the most prominent observation is the higher peak intensity of metallic Ni than those of the respective reduced catalysts. This indicates that the Ni sintering apparently occurs over the catalyst evaluated for CRM, the extent of which is closely associated with the complexing agent used for the synthesis of the catalyst. To quantitatively estimate the extent of the metallic Ni sintering, the spent catalysts were subjected to TEM observations, and the results are given in Figure 5. In comparison with the results of the reduced catalysts (D1, E1, and G1 in Figure S2), the spent  $\text{Ni}_{0.1}\text{Mg}_{0.9}\text{O}$ -800-Pro,  $\text{Ni}_{0.1}\text{Mg}_{0.9}\text{O}$ -800-Ser, and  $\text{Ni}_{0.1}\text{Mg}_{0.9}\text{O}$ -800-Ala catalysts showed an obvious sintering, i.e., broader size distributions of metallic Ni particles with average sizes of  $16.7 \pm 2.3$ ,  $10.5 \pm 1.0$ , and  $14.4 \pm 1.2\text{ nm}$ , which are much larger than those of the reduced catalyst of  $4.1 \pm 0.3$ ,  $3.5 \pm 0.3$ , and  $4.2 \pm 0.3\text{ nm}$ , respectively. In contrast, much similarly narrower size distributions of Ni particles around 6–10 nm were observed for the remaining spent catalysts, which were also similar to those of the reduced counterparts (about 1.5–5.0 nm, Figure S2 (A1,B1,C1,F1)). However, the average size of the metallic Ni particles over these spent catalysts ( $7.6\text{--}7.9 \pm 0.5\text{--}0.6\text{ nm}$ ) was almost double that of the reduced catalysts ( $3.2\text{--}3.4 \pm 0.2\text{--}0.6\text{ nm}$ ). Thus, the Ni sintering during CRM over  $\text{Ni}_{0.1}\text{Mg}_{0.9}\text{O}$ -800-Gly,  $\text{Ni}_{0.1}\text{Mg}_{0.9}\text{O}$ -800-Gla,  $\text{Ni}_{0.1}\text{Mg}_{0.9}\text{O}$ -800-Oxa, and  $\text{Ni}_{0.1}\text{Mg}_{0.9}\text{O}$ -800-Urea were effectively inhibited compared with that over  $\text{Ni}_{0.1}\text{Mg}_{0.9}\text{O}$ -800-Pro,  $\text{Ni}_{0.1}\text{Mg}_{0.9}\text{O}$ -800-Ser, and  $\text{Ni}_{0.1}\text{Mg}_{0.9}\text{O}$ -800-Ala.

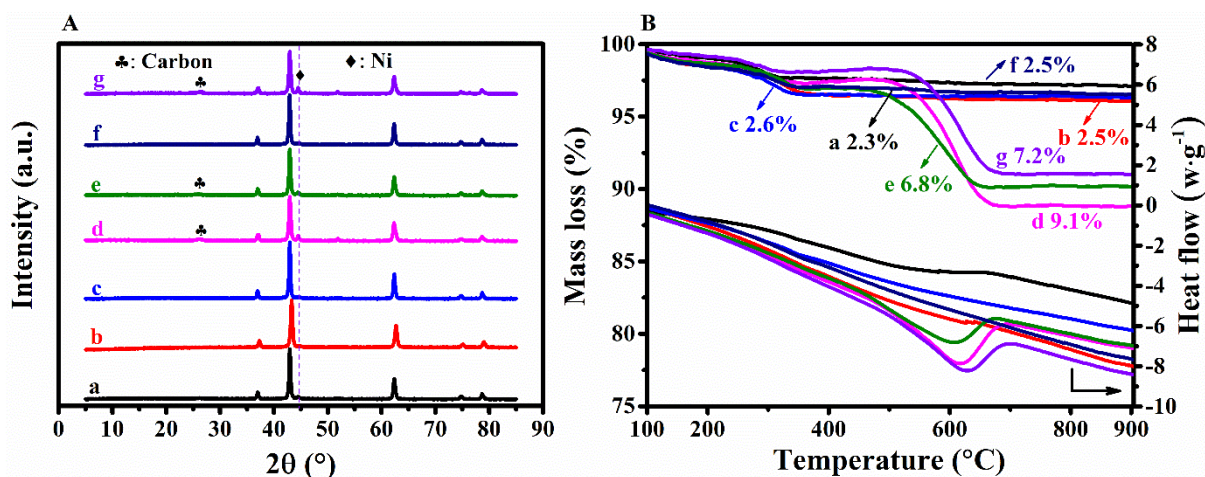


**Figure 4.** XRD patterns (A) and TG-DSC curves (B) for the spent catalysts of Ni<sub>0.1</sub>Mg<sub>0.9</sub>O-800-Gly (a), Ni<sub>0.1</sub>Mg<sub>0.9</sub>O-800-Gla (b), Ni<sub>0.1</sub>Mg<sub>0.9</sub>O-800-Oxa (c), Ni<sub>0.1</sub>Mg<sub>0.9</sub>O-800-Pro (d), Ni<sub>0.1</sub>Mg<sub>0.9</sub>O-800-Ser (e), Ni<sub>0.1</sub>Mg<sub>0.9</sub>O-800-Urea (f), Ni<sub>0.1</sub>Mg<sub>0.9</sub>O-800-Ala (g).

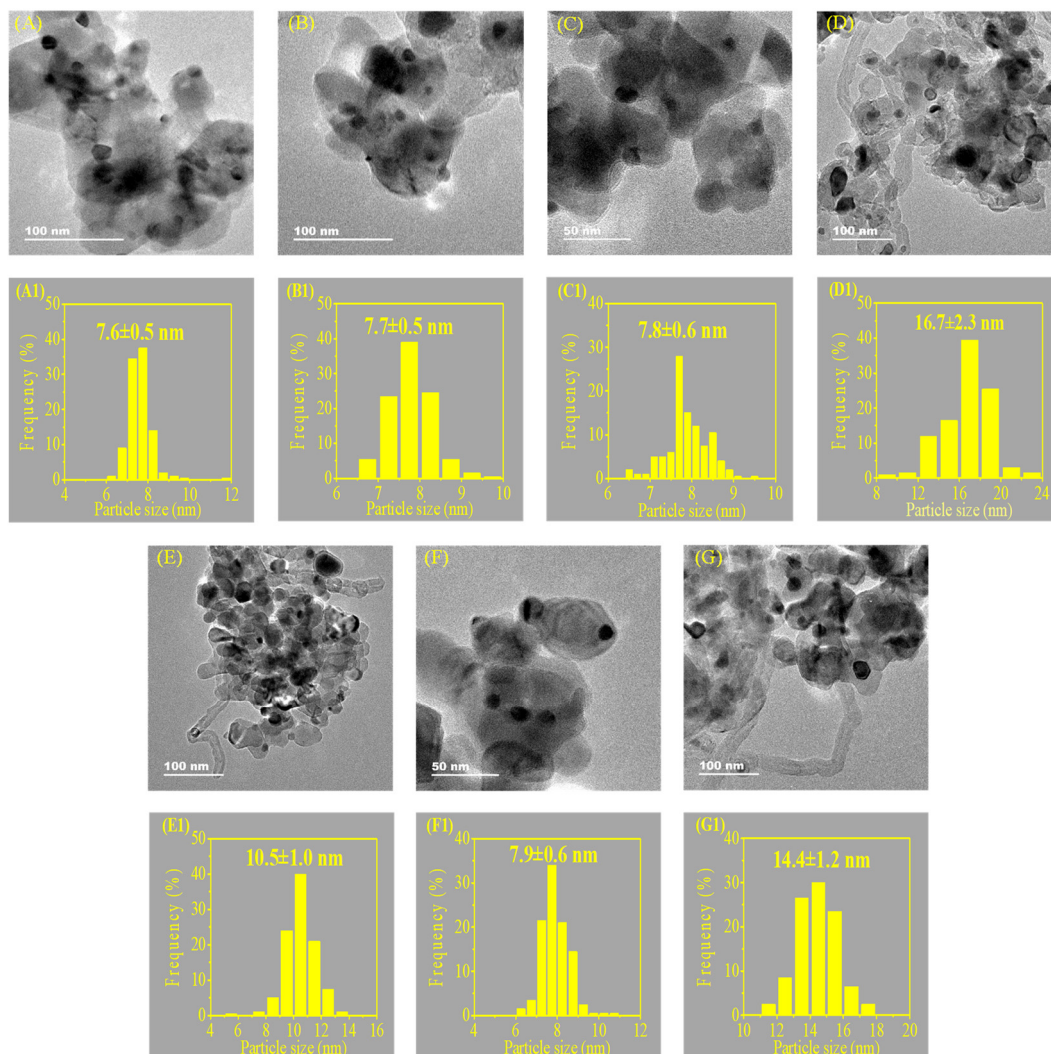


**Figure 5.** TEM images and corresponding particle-size distribution for the spent catalysts of Ni<sub>0.1</sub>Mg<sub>0.9</sub>O-800-Gly (A,A1), Ni<sub>0.1</sub>Mg<sub>0.9</sub>O-800-Gla (B,B1), Ni<sub>0.1</sub>Mg<sub>0.9</sub>O-800-Oxa (C,C1), Ni<sub>0.1</sub>Mg<sub>0.9</sub>O-800-Pro (D,D1), Ni<sub>0.1</sub>Mg<sub>0.9</sub>O-800-Ser (E,E1), Ni<sub>0.1</sub>Mg<sub>0.9</sub>O-800-Urea (F,F1), Ni<sub>0.1</sub>Mg<sub>0.9</sub>O-800-Ala (G,G1).

In addition to the metallic Ni, the other obvious phenomenon is the appearance of a new XRD diffraction at about  $26^\circ$  for the spent  $\text{Ni}_{0.1}\text{Mg}_{0.9}\text{O}$ -800-Pro,  $\text{Ni}_{0.1}\text{Mg}_{0.9}\text{O}$ -800-Ser, and  $\text{Ni}_{0.1}\text{Mg}_{0.9}\text{O}$ -800-Ala samples. This can be reasonably assigned to the diffraction of graphitized carbon, since carbon nanotubes are clearly found over these spent catalysts (Figure 5D,E,G). Moreover, this is further confirmed from the TG-DSC results given in Figure 4B. Indeed, the weight loss above  $300^\circ\text{C}$  for the spent catalysts was decreased in the order of  $\text{Ni}_{0.1}\text{Mg}_{0.9}\text{O}$ -800-Pro >  $\text{Ni}_{0.1}\text{Mg}_{0.9}\text{O}$ -800-Ala >  $\text{Ni}_{0.1}\text{Mg}_{0.9}\text{O}$ -800-Ser >>  $\text{Ni}_{0.1}\text{Mg}_{0.9}\text{O}$ -800-Oxa  $\approx$   $\text{Ni}_{0.1}\text{Mg}_{0.9}\text{O}$ -800-Gla  $\approx$   $\text{Ni}_{0.1}\text{Mg}_{0.9}\text{O}$ -800-Urea >  $\text{Ni}_{0.1}\text{Mg}_{0.9}\text{O}$ -800-Gly. This is consistent with the DSC curves of the catalysts (Figure 4B), in which large exothermal peaks were obtained for the samples with significant weight losses. Quantitatively, the coke content over the spent  $\text{Ni}_{0.1}\text{Mg}_{0.9}\text{O}$ -800-Pro,  $\text{Ni}_{0.1}\text{Mg}_{0.9}\text{O}$ -800-Ser, and  $\text{Ni}_{0.1}\text{Mg}_{0.9}\text{O}$ -800-Ala was determined to be 9.1, 6.8, and 7.2 wt.%, respectively, which is significantly higher than those of the remaining catalyst (2.3–2.6 wt.%). Hence, the coke deposition is effectively suppressed over  $\text{Ni}_{0.1}\text{Mg}_{0.9}\text{O}$ -800-Gly,  $\text{Ni}_{0.1}\text{Mg}_{0.9}\text{O}$ -800-Gla,  $\text{Ni}_{0.1}\text{Mg}_{0.9}\text{O}$ -800-Oxa, and  $\text{Ni}_{0.1}\text{Mg}_{0.9}\text{O}$ -800-Urea.

### 3.4. Impact of Preparation Parameters of NiO-MgO on CRM Performance

In order to obtain the relationship between NiO-MgO solid solution and the CRM performance, the representative catalysts prepared by using glycine as complexing agent with different calcination temperatures and Ni/Mg molar ratios were characterized by XRD,  $\text{H}_2$ -TPR, and TG-DSC, and evaluated for CRM.

Regardless of the calcination temperatures, NiO-MgO solid solution was formed on all of the catalysts (Figure S3A), but the crystallinity was gradually increased with increasing the calcination temperature (Figure 6A). Moreover, the diffraction at  $43^\circ$  gradually shifted to the higher diffraction angle. This result can be explained by the promotional effect of the elevated calcination temperature on forming NiO-MgO solid solution. As revealed from Figure S3B, metallic Ni particles over the reduced  $\text{Ni}_{0.1}\text{Mg}_{0.9}\text{O}$ -600-Gly and  $\text{Ni}_{0.1}\text{Mg}_{0.9}\text{O}$ -700-Gly catalysts were larger, as revealed by the sharper XRD diffractions of metallic Ni. In contrast, these diffractions were not detected on the XRD patterns of the reduced  $\text{Ni}_{0.1}\text{Mg}_{0.9}\text{O}$ -800-Gly and  $\text{Ni}_{0.1}\text{Mg}_{0.9}\text{O}$ -900-Gly samples, indicating better dispersion. The larger Ni particles are attributed to the reduction of the weakly bound NiO species, which were predominant under relatively lower calcination temperatures of  $600$ – $700^\circ\text{C}$  (Figure 6B). It should be noted that the amount of the weakly bound NiO species gradually decreased and finally disappeared with increasing the calcination temperature from  $600$  to  $800^\circ\text{C}$ . If the calcination temperature was further increased to  $900^\circ\text{C}$ , a similar trend was found for the reduction of the strongly bound NiO species ( $\sim 565^\circ\text{C}$ ). Moreover, a gradual shift to a higher temperature ( $811$ ,  $841$ , and  $895^\circ\text{C}$ ) was observed for the reduction of NiO-MgO solid solution. These phenomena prove that increasing the calcination temperature enhances the interactions between NiO and MgO, which can be explained as the faster diffusion of  $\text{Ni}^{2+}$  into the MgO lattice at higher calcination temperatures.

As indicated from the TOS results of CRM shown in Figure S4A,  $\text{Ni}_{0.1}\text{Mg}_{0.9}\text{O}$ -600-Gly,  $\text{Ni}_{0.1}\text{Mg}_{0.9}\text{O}$ -700-Gly, and  $\text{Ni}_{0.1}\text{Mg}_{0.9}\text{O}$ -800-Gly exhibited a stable  $\text{CH}_4$  conversion, although it was slightly higher over  $\text{Ni}_{0.1}\text{Mg}_{0.9}\text{O}$ -800-Gly. In contrast, the  $\text{CH}_4$  conversion over  $\text{Ni}_{0.1}\text{Mg}_{0.9}\text{O}$ -900-Gly gradually increased from 65 to 83% with increasing TOS from 1 to 15 h, and was then kept constant until the end of the test. A similar phenomenon has been reported on the methanol stream reforming over Cu-Al spinel catalysts [27], the mechanisms of which are explained by that active Cu is gradually released via the in situ reduction of the non-spinel  $\text{Cu}^{2+}$  species in the spinel structure. This explanation may also be applicable in the case of  $\text{Ni}_{0.1}\text{Mg}_{0.9}\text{O}$ -900-Gly, which will be discussed later.

As revealed from Figure S5A and Figure 7A, the shift in the XRD diffraction to a higher angle became more obvious for the catalyst with a higher Ni/MgO molar ratio, suggesting that more  $\text{Ni}^{2+}$  cations are diffused into the MgO lattice to form NiO-MgO solid solution. When the Ni/Mg molar ratio was higher than 15/85, the free NiO species were formed on the catalysts, as confirmed by the individual diffraction of NiO. As a result, the reduced

$\text{Ni}_{0.15}\text{Mg}_{0.85}\text{O}$ -800-Gly and  $\text{Ni}_{0.20}\text{Mg}_{0.80}\text{O}$ -800-Gly showed obvious diffractions of metallic Ni (Figure S5B), attributable to the larger Ni particles.  $\text{H}_2$ -TPR profiles showed that strongly bound NiO species and NiO-MgO solid solution co-existed on the catalysts (Figure 7B). Moreover, the content of strongly bound NiO species gradually decreased, but that of NiO-MgO solid solution increased with increasing Ni/Mg molar ratios. This was also confirmed by the varied  $\text{H}_2$  consumption for the respective reduction peak. Apparently, changing the Ni/Mg molar ratio only alters the content of NiO species and NiO-MgO solid solution, but does not exert influence on the interactions between NiO and MgO.

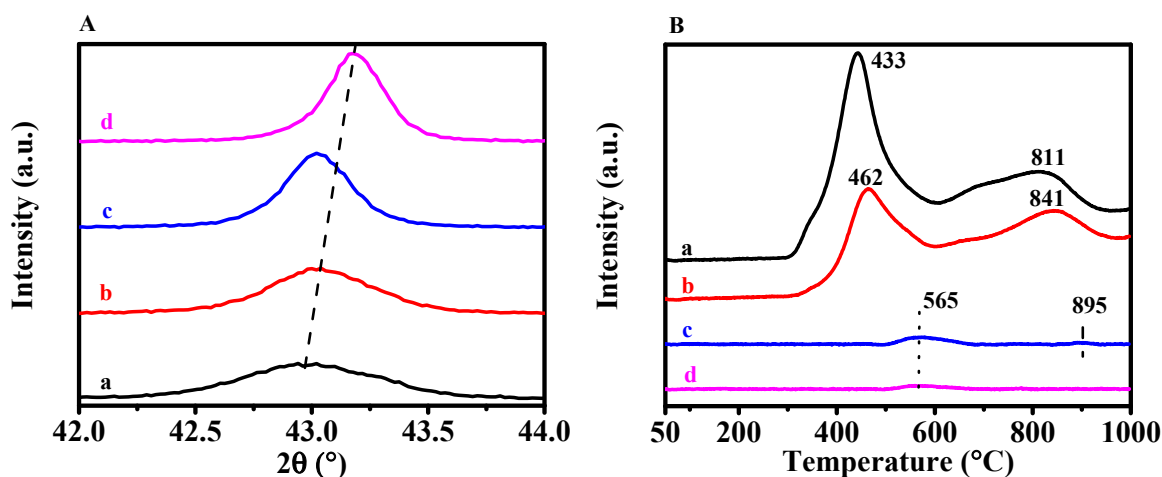


**Figure 6.** XRD patterns (A) and  $\text{H}_2$ -TPR profiles (B) for the fresh catalysts of  $\text{Ni}_{0.1}\text{Mg}_{0.9}\text{O}$ -Gly-600 (a),  $\text{Ni}_{0.1}\text{Mg}_{0.9}\text{O}$ -Gly-700 (b),  $\text{Ni}_{0.1}\text{Mg}_{0.9}\text{O}$ -Gly-800 (c),  $\text{Ni}_{0.1}\text{Mg}_{0.9}\text{O}$ -Gly-900 (d).

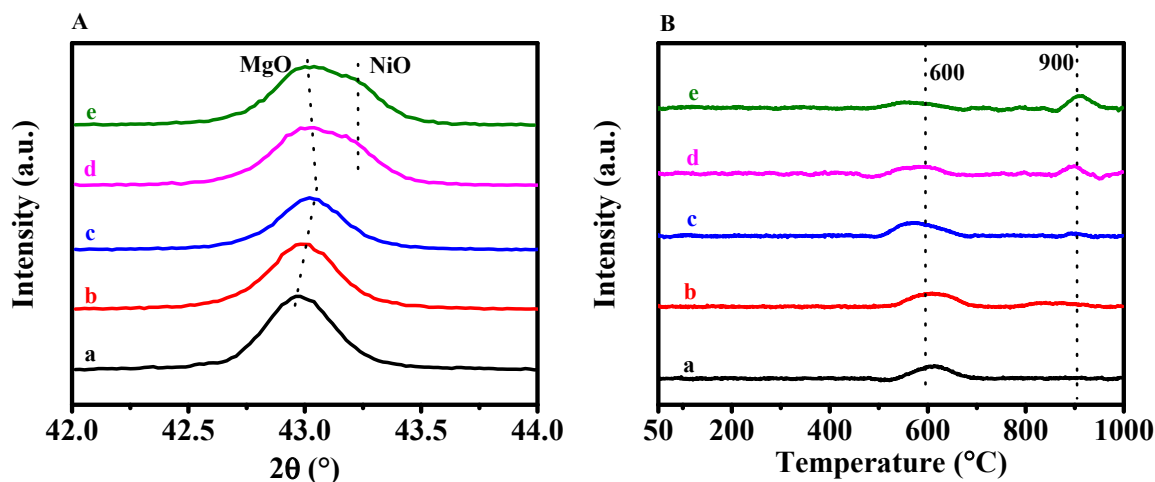


**Figure 7.** XRD patterns (A) and  $\text{H}_2$ -TPR profiles (B) for the fresh catalysts of  $\text{Ni}_{0.05}\text{Mg}_{0.95}\text{O}$ -800-Gly (a),  $\text{Ni}_{0.07}\text{Mg}_{0.93}\text{O}$ -800-Gly (b),  $\text{Ni}_{0.10}\text{Mg}_{0.90}\text{O}$ -800-Gly (c),  $\text{Ni}_{0.15}\text{Mg}_{0.85}\text{O}$ -800-Gly (d),  $\text{Ni}_{0.20}\text{Mg}_{0.80}\text{O}$ -800-Gly (e).

As for the TOS results of CRM over these catalysts, the initial  $\text{CH}_4$  conversion was gradually increased with increasing the Ni/Mg molar ratio over the catalysts, and  $\text{Ni}_{0.15}\text{Mg}_{0.85}\text{O}$ -800-Gly and  $\text{Ni}_{0.20}\text{Mg}_{0.80}\text{O}$ -800-Gly exhibited the highest  $\text{CH}_4$  conversion, which was kept stable for a TOS of 20 h (Figure S4B). The varied CRM activities over different catalysts can be well explained by the increased Ni loading. However, in the cases of  $\text{Ni}_{0.05}\text{Mg}_{0.95}\text{O}$ -800-Gly,  $\text{Ni}_{0.07}\text{Mg}_{0.93}\text{O}$ -800-Gly, and  $\text{Ni}_{0.10}\text{Mg}_{0.90}\text{O}$ -800-Gly with slightly varied Ni loadings, the gradual increase in the activity can be mainly attributed to the in situ reduction of the difficultly reducible NiO-MgO solid solution under CRM conditions, which can supply extra active sites of metallic Ni.

#### 4. Discussion

From the characterization and CRM results, the initial CH<sub>4</sub> conversion and the TOS stability are significantly affected by the synthesis parameters, i.e., the complexing agent, the calcination temperature, and the Ni/Mg molar ratio, of the catalysts, which are induced from the characteristics of the Ni species and the interactions between Ni and MgO in the NiO-MgO solid solutions. Therefore, in order to testify to the corresponding effect, more detailed discussions are made as follows.

Ni<sub>0.1</sub>Mg<sub>0.9</sub>O-800-Y showed high activity for CRM with initial CH<sub>4</sub> conversions of 80–86%. Considering the difficulty in reducing NiO-MgO solid solution (Figure 2), the initially active Ni mainly originated from the readily reducible NiO species during the pre-treatment of H<sub>2</sub> reduction. Apparently, the complexing agents significantly alter the amounts of the readily reducible NiO species (weakly and strongly bound NiO) over the catalysts, as confirmed by the varied H<sub>2</sub> consumptions (Figure 2). More importantly, the difference in the coordinative capacity of the complexing agents led to the varied Ni dispersions, which were significantly responsible for the different initial activities. This result can be well supported by the fact that the Ni<sub>0.1</sub>Mg<sub>0.9</sub>O catalysts prepared by glycine and oxalic acid, with stronger coordinative capacity, show a higher activity than those prepared with inferior coordinative capacity (Figures 1A and 3A). Furthermore, no obvious correlation between the initial activity and the textural properties was shown for all of the catalysts (Table 1 and Figure 3). This result suggests that the textural properties adjusted by the complexing agents hardly affect the activity compared to the Ni dispersion. As for Ni<sub>0.1</sub>Mg<sub>0.9</sub>O-T-Gly, the amount of the readily reducible NiO species increased with decreasing the calcination temperature (Figure 6B). Thus, the initially high CH<sub>4</sub> conversion was achieved over the catalysts calcined at lower temperatures (Figure S4A). When the Ni/Mg molar ratio was examined, the significantly varied activities were easily attributed to the relatively larger changes in Ni content over the catalysts (Figure S4B).

According to the results of characterization and CRM evaluation, one can be found that the initial CH<sub>4</sub> conversion depends on the amount of the Ni active sites, which are mainly originated from the readily reducible NiO species. However, the change in activity is significantly related to the release of metallic Ni from the in situ reduction of NiO-MgO solid solution under CRM conditions. A gradual increase in activity was shown for Ni<sub>0.1</sub>Mg<sub>0.9</sub>O-800-Gly and Ni<sub>0.1</sub>Mg<sub>0.9</sub>O-900-Gly, but the increase rate of Ni<sub>0.1</sub>Mg<sub>0.9</sub>O-800-Gly was faster than that of Ni<sub>0.1</sub>Mg<sub>0.9</sub>O-900-Gly. Therefore, the activity for Ni<sub>0.1</sub>Mg<sub>0.9</sub>O-800-Gly rapidly tended to be stable; however, that of Ni<sub>0.1</sub>Mg<sub>0.9</sub>O-900-Gly continuously increased in a TOS of 20 h. If the varied interactions between NiO and MgO are considered, this phenomenon can be easily explained as because the stronger interaction between NiO and MgO on Ni<sub>0.1</sub>Mg<sub>0.9</sub>O-900-Gly causes a lower release rate of active Ni during CRM compared to Ni<sub>0.1</sub>Mg<sub>0.9</sub>O-800-Gly (Figure 6B). When the Ni/Mg molar ratio was changed, the difference in the reduction behaviors was not obvious (Figure 7B). However, more Ni<sup>2+</sup> ions diffused into the MgO lattice by increasing the Ni/Mg molar ratio, leading to the NiO-MgO solid solution. In this context, the amounts of released Ni over the catalysts with a high Ni/Mg molar ratio are larger than that with a low Ni/Mg molar ratio. Therefore, the increase rates of the activity were different over Ni<sub>x</sub>Mg<sub>1-x</sub>O-800-Gly (Figure S4B).

Generally, the sintering of metallic Ni and coke deposition, leading to the decrease in active Ni, are the main factors for the decay of CRM [11,28]. In this work, the loss of the initially active Ni was caused by the sintering and coke deposition, whereas the active Ni could be compensated from the in situ reduction in NiO-MgO solid solution during the CRM process. Therefore, the relationship between the loss of initially active Ni and the compensation of active Ni is significantly responsible for the stability. In the case of Ni<sub>0.1</sub>Mg<sub>0.9</sub>O-600-Gly and Ni<sub>0.1</sub>Mg<sub>0.9</sub>O-700-Gly, the larger Ni particles (Figure S3B) are beneficial to the formation of cokes [29], and the weakly bound NiO species were predominant on the two catalysts (Figure 6D), which encountered serious sintering (Figure S6A). Thus, the loss rate of active Ni is larger than the release rate of active Ni, resulting in a linear decay of activity over Ni<sub>0.1</sub>Mg<sub>0.9</sub>O-600-Gly and Ni<sub>0.1</sub>Mg<sub>0.9</sub>O-700-Gly. In contrast,

the high Ni dispersion (smaller Ni particles, Figure S2A) and the relatively strong metal-support interaction (Figures 2 and 6B) were shown for  $\text{Ni}_{0.1}\text{Mg}_{0.9}\text{O}$ -800-Gly, effectively suppressing the sintering (Figure 5A) and coke deposition (Figures 4B and S6A), which caused a lower loss rate of active Ni. Therefore, good stability was achieved on this catalyst by constructing a balance between the loss and release rates of active Ni. Moreover, the released Ni with strong metal-support interaction probably possesses better anti-sintering and anti-coking capacities, which also contribute to the high stability of  $\text{Ni}_{0.1}\text{Mg}_{0.9}\text{O}$ -800-Gly. In the cases of  $\text{Ni}_{0.15}\text{Mg}_{0.85}\text{O}$ -800-Gly and  $\text{Ni}_{0.20}\text{Mg}_{0.80}\text{O}$ -800-Gly, the loss rate of active Ni was relatively higher than the release rate, resulting in the slight decrease in activities (Figure S4B).

On the basis of the above discussion, reasonable explanations for the difference in stability over  $\text{Ni}_{0.1}\text{Mg}_{0.9}\text{O}$  prepared with different complexing agents are provided. In the cases of  $\text{Ni}_{0.1}\text{Mg}_{0.9}\text{O}$ -800-Pro and  $\text{Ni}_{0.1}\text{Mg}_{0.9}\text{O}$ -800-Ala, the larger Ni particles promoted coke deposition (Figure 4B), and these gains with relatively weak metal-support interaction showed inferior anti-sintering capacity (Figure 5D,G). Therefore, the serious sintering and coke deposition lead to a larger loss rate of active Ni than the release rate, causing an obvious deactivation at the initial stage of CRM (Figure 3A). Moreover, a balance between the loss and release rates can be achieved by prolonging the TOS, and hence, the activities keep constant. As for  $\text{Ni}_{0.1}\text{Mg}_{0.9}\text{O}$ -800-Ser, the linear deactivation is also attributed to the mismatch between the loss and release rates, the explanation for which is that the serious sintering and coke deposition (Figures 4B and 5E) cause a larger loss rate of active Ni. In the cases of  $\text{Ni}_{0.1}\text{Mg}_{0.9}\text{O}$ -800-Gla,  $\text{Ni}_{0.1}\text{Mg}_{0.9}\text{O}$ -800-Oxa, and  $\text{Ni}_{0.1}\text{Mg}_{0.9}\text{O}$ -800-Urea, the relatively slower loss rate of active Ni is achieved, attributable to the lower sintering and coke deposition (Figures 4B and 5A–C,F), which is conducive to constructing a balance between the loss and release rates of active Ni, resulting in a stable activity.

Apparently, the complexing agents, calcination temperature, and Ni/Mg molar ratio can exert a significant influence on the CRM performance over the NiO-MgO catalysts prepared by the complex-decomposition method. The initial  $\text{CH}_4$  conversion depends on the initially active Ni, which mainly originates from the reduction of the readily reducible NiO species. When the complexing agents are carefully compared, a stronger coordinative capacity is shown for glycine, glacial acetic acid, oxalic acid, and urea, leading to the higher Ni dispersion, which causes the highly initial activities. Moreover, the loss rate of the initially active Ni is significantly associated with its anti-sintering and anti-coking capacities, which can be adjusted by changing the complexing agents, calcination temperature, and Ni/Mg molar ratio. On the other hand, the varied coordinative capacities of the complexing agents also affect the formed NiO-MgO solid solution and the interaction between NiO and MgO, which can adjust the release rate of active Ni via the in situ reduction of NiO-MgO solid solution. Similarly, the release rate of active Ni is adjusted by changing the calcination temperature and Ni/Mg molar ratio. Therefore, constructing a balance between the loss and release rates of active Ni via changing the complexing agent, calcination temperature, and Ni/MgO is crucial for the highly catalytic stability. Combining the characterization results with the CRM performance, a good balance between the loss and release rates of active Ni is achieved over the  $\text{Ni}_{0.1}\text{Mg}_{0.9}\text{O}$ -800-Gly, leading to a highly catalytic stability. Overall, the suitable complexing agent, calcination temperature, and Ni/Mg molar ratio are the essential factors for preparing a high-performance NiO-MgO catalyst via the complex-decomposition method.

To demonstrate the high performance of the developed catalysts, the CRM performance of the optimal  $\text{Ni}_{0.1}\text{Mg}_{0.9}\text{O}$ -800-Gly catalyst together with the main reaction conditions is compared with those of the representative Ni-based catalysts reported in the recent literatures [5,30–34]. As shown in Table S1,  $\text{Ni}_{0.1}\text{Mg}_{0.9}\text{O}$ -800-Gly shows similarly high and even better CRM activity than those of the most Ni-based catalysts. For example,  $\text{Ni}_{0.1}\text{Mg}_{0.9}\text{O}$ -800-Gly exhibits almost the same specific activity as Ni/SBA-15 (11.5 vs. 11.4  $\text{mol}\cdot\text{g}^{-1}\cdot\text{h}^{-1}$ ), and is only lower than that of Ni/La<sub>2</sub>O<sub>2</sub>CO<sub>3</sub>-Al<sub>2</sub>O<sub>3</sub>, which is evaluated for CRM with significantly diluted reactants. Moreover,  $\text{Ni}_{0.1}\text{Mg}_{0.9}\text{O}$ -800-Gly shows

a similarly high stability to those of the compared catalysts. This vigorously confirms that the complex-decomposition method is a convenient and promising strategy to prepare high-performance NiO-MgO catalysts. Considering the low cost of the precursor of nickel, magnesium and the complexing agent, the NiO-MgO catalyst has the potential for large-scale preparation.

## 5. Conclusions

In summary, the complexing agents, calcination temperature, and Ni/Mg molar ratio exerted significant influence on the phase composition, Ni dispersion, and interaction between NiO and MgO over the catalysts. As a result of the strong coordination between glycine and  $\text{Ni}^{2+}$ , the highest initial  $\text{CH}_4$  conversion of CRM over the NiO-MgO catalyst prepared by using glycine as the complexing agent was obtained (~86%), which could be mainly ascribed to the highest Ni dispersion over the catalyst. Moreover, with increasing the coordinative capacity of the complexing agent,  $\text{Ni}^{2+}$  diffusing into the MgO lattice was increasingly promoted for the formation of the NiO-MgO solid solution. Importantly, due to varied interactions between NiO and MgO over the catalysts, rates for the in situ release of metallic Ni under CRM reaction conditions were varied. In this case, the catalytic stability was obviously dependent on the relationship between the loss of metallic Ni due to sintering and the release of metallic Ni originated from the in situ reduction of NiO-MgO solid solution under CRM conditions. As a result of the good balance of these two factors, the  $\text{Ni}_{0.1}\text{Mg}_{0.9}\text{O}$  catalyst prepared by using glycine as the complexing agent and calcined at 800 °C showed the best catalytic stability. Considering the simple procedure of the complex-decomposition method and the conveniently adjustable properties of the NiO-MgO catalysts by simply changing the complexing agents, calcination temperature, and Ni/Mg molar ratio, the thus developed catalyst can be used to better understand the CRM mechanisms and extend their use to large-scale preparation.

**Supplementary Materials:** The following supporting information can be downloaded at: <https://www.mdpi.com/article/10.3390/pr11020596/s1>, Figure S1:  $\text{N}_2$  isotherms; Figure S2: TEM images of reduced catalysts; Figure S3: XRD patterns of the  $\text{Ni}_{0.1}\text{Mg}_{0.9}\text{O}$ -Gly-T catalysts; Figure S4:  $\text{CH}_4$  conversions of the catalysts; Figure S5: XRD patterns of the  $\text{Ni}_x\text{Mg}_{1-x}\text{O}$ -800-Gly catalysts; Figure S6: TG curves and XRD patterns of the spent  $\text{Ni}_{0.1}\text{Mg}_{0.9}\text{O}$ -T-Gly catalysts; Figure S7: TG curves and XRD patterns of the spent  $\text{Ni}_x\text{Mg}_{1-x}\text{O}$ -800-Gly catalysts; Table S1: Summarized reaction conditions and the typical CRM results of the optimal NiO-MgO and the representatively reported Ni-based catalysts.

**Author Contributions:** Conceptualization and methodology, Z.-W.L.; experimental data curation, Y.W. and Y.-S.X.; writing—original draft preparation, Y.W., B.L. and Y.-S.X.; writing—review and editing, Z.-W.L.; supervision, Z.-W.L. All authors have read and agreed to the published version of the manuscript.

**Funding:** This research was funded by the National Natural Science Foundation of China (U1862116) and the Fundamental Research Funds for the Central Universities (GK201901001).

**Data Availability Statement:** All data are reported in the paper.

**Acknowledgments:** The financial supports from the National Natural Science Foundation of China (U1862116) and the Fundamental Research Funds for the Central Universities (GK201901001) are highly appreciated.

**Conflicts of Interest:** The authors declare no conflict of interest.

## References

1. Li, M.J.; Sun, Z.X.; Hu, Y.H. Catalysts for  $\text{CO}_2$  reforming of  $\text{CH}_4$ : A review. *J. Mater. Chem. A* **2021**, *9*, 12495. [CrossRef]
2. Abdulrasheed, A.; Jalil, A.A.; Gambo, Y.; Ibrahim, M.; Hambali, H.U.; Shahul Hamid, M.Y. A review on catalyst development for dry reforming of methane to syngas: Recent advances. *Renew. Sustain. Energy Rev.* **2019**, *108*, 175–193. [CrossRef]
3. Sinh, R.; Dhir, A.; Mohapatra, S.K.; Mahla, S.K. Dry reforming of methane using various catalysts in the process: Review. *Biomass. Conv. Bioref.* **2019**, *10*, 567–587. [CrossRef]

4. Li, Z.W.; Lin, Q.; Li, M.; Cao, J.X.; Liu, F.; Pan, H.Y.; Wang, Z.G.; Kawi, S. Recent advances in process and catalyst for CO<sub>2</sub> reforming of methane. *Renew. Sustain. Energy Rev.* **2020**, *134*, 110312. [[CrossRef](#)]
5. Bacariza, C.; Karam, L.; Hassan, N.E.; Lopes, J.M.; Henriques, C. Carbon dioxide reforming of methane over nickel-supported zeolites: A screening study. *Processes* **2022**, *10*, 1331. [[CrossRef](#)]
6. Azizi, Z.; Rezaeimanesh, M.; Tohidian, T.; Rahimpour, M.R. Dimethyl ether: A review of technologies and production challenges. *Chem. Eng. Process.* **2014**, *82*, 150–172. [[CrossRef](#)]
7. San-José-Alonso, D.; Juan-Juan, J.; Illán-Gómez, M.J.; Román-Martínez, M.C. Ni, Co and bimetallic Ni–Co catalysts for the dry reforming of methane. *Appl. Catal. A Gen.* **2009**, *371*, 54–59. [[CrossRef](#)]
8. Wang, N.; Yu, X.; Wang, Y.; Chu, W.; Liu, M. A comparison study on methane dry reforming with carbon dioxide over LaNiO<sub>3</sub> perovskite catalysts supported on mesoporous SBA-15, MCM-41 and silica carrier. *Catal. Today* **2013**, *212*, 98–107. [[CrossRef](#)]
9. Sajjadi, S.M.; Haghighi, M.; Eshghi, J. Synergic influence of potassium loading and plasma-treatment on anti-coke property of K-promoted bimetallic NiCo–NiAl<sub>2</sub>O<sub>4</sub> nanocatalyst applied in O<sub>2</sub>-enhanced dry reforming of CH<sub>4</sub>. *Int. J. Hydrogen Energy* **2019**, *44*, 13397–13414. [[CrossRef](#)]
10. Liu, C.J.; Ye, J.; Jiang, J.; Pan, Y. Progresses in the Preparation of Coke Resistant Ni-based Catalyst for Steam and CO<sub>2</sub> Reforming of Methane. *ChemCatChem* **2011**, *3*, 529–541. [[CrossRef](#)]
11. Sajjadi, S.M.; Haghighi, M.; Rahmani, F.; Eshghi, J. Plasma-enhanced sol-gel fabrication of CoWNiAl<sub>2</sub>O<sub>4</sub> nanocatalyst used in oxidative conversion of greenhouse CH<sub>4</sub>/CO<sub>2</sub> gas mixture to H<sub>2</sub>/CO. *J. CO<sub>2</sub> Util.* **2022**, *61*, 102037. [[CrossRef](#)]
12. Abdullah, B.; Abd Ghani, N.A.; Vo, D.V.N. Recent advances in dry reforming of methane over Ni-based catalysts. *J. Clean. Prod.* **2017**, *162*, 170–185. [[CrossRef](#)]
13. Salaev, M.A.; Liotta, L.F.; Vodyankina, O.V. Lanthanoid-containing Ni-based catalysts for dry reforming of methane: A review. *Int. J. Hydrogen Energy* **2022**, *47*, 4489–4535. [[CrossRef](#)]
14. Ren, H.-P.; Song, Y.-H.; Wang, W.; Chen, J.-G.; Cheng, J.; Jiang, J.; Liu, Z.-T.; Liu, Z.-W.; Hao, Z.; Lu, J. Insights into CeO<sub>2</sub>-modified Ni–Mg–Al oxides for pressurized carbon dioxide reforming of methane. *Chem. Eng. J.* **2015**, *259*, 581–593. [[CrossRef](#)]
15. Xu, L.; Song, H.; Chou, L. One-Pot Synthesis of Ordered Mesoporous NiO–CaO–Al<sub>2</sub>O<sub>3</sub> Composite Oxides for Catalyzing CO<sub>2</sub> Reforming of CH<sub>4</sub>. *ACS Catal.* **2012**, *2*, 1331–1342. [[CrossRef](#)]
16. Yang, R.; Xing, C.; Lv, C.; Shi, L.; Tsubaki, N. Promotional effect of La<sub>2</sub>O<sub>3</sub> and CeO<sub>2</sub> on Ni/γ-Al<sub>2</sub>O<sub>3</sub> catalysts for CO<sub>2</sub> reforming of CH<sub>4</sub>. *Appl. Catal. A Gen.* **2010**, *385*, 92–100. [[CrossRef](#)]
17. Akri, M.; Zhao, S.; Li, X.; Zang, K.; Lee, A.F.; Isaacs, M.A.; Xi, W.; Gangarajula, Y.; Luo, J.; Ren, Y.; et al. Atomically dispersed nickel as coke-resistant active sites for methane dry reforming. *Nat. Commun.* **2019**, *10*, 5181. [[CrossRef](#)]
18. Zuo, Z.; Liu, S.; Wang, Z.; Liu, C.; Huang, W.; Huang, J.; Liu, P. Dry Reforming of Methane on Single-Site Ni/MgO Catalysts: Importance of Site Confinement. *ACS Catal.* **2018**, *8*, 9821–9835. [[CrossRef](#)]
19. Song, Y.D.; Ramesh, S.; Adishev, A.; Subramanian, S.; Harale, A.; Albuali, M.; Fadhel, B.A.; Jamal, A.; Moon, D.; Choi, S.H.; et al. Dry reforming of methane by stable Ni–Mo nanocatalysts on single-crystalline MgO. *Science* **2020**, *367*, 777–781. [[CrossRef](#)]
20. Ruckenstein, E.; Hu, Y.H. Carbon dioxide reforming of methane over nickel/alkaline earth metal oxide catalysts. *Appl. Catal. A Gen.* **1995**, *133*, 149–161. [[CrossRef](#)]
21. Kuzmin, A.; Mironova, N. Composition dependence of the lattice parameter in Ni<sub>c</sub>Mg<sub>1–c</sub>O solid solutions. *J. Phys. Condens. Mat.* **1998**, *10*, 7937–7944. [[CrossRef](#)]
22. Ren, H.-P.; Hao, Q.-Q.; Wang, W.; Song, Y.-H.; Cheng, J.; Liu, Z.-W.; Liu, Z.-T.; Lu, J.; Hao, Z. High-performance Ni–SiO<sub>2</sub> for pressurized carbon dioxide reforming of methane. *Int. J. Hydrogen Energy* **2014**, *39*, 11592–11605. [[CrossRef](#)]
23. Qin, P.; Xu, H.; Long, H.; Ran, Y.; Shang, S.; Yin, Y.; Dai, X. Ni/MgO catalyst prepared using atmospheric high-frequency discharge plasma for CO<sub>2</sub> reforming of methane. *J. Nat. Gas Chem.* **2011**, *20*, 487–492. [[CrossRef](#)]
24. Wang, Y.-H.; Liu, H.-M.; Xu, B.-Q. Durable Ni/MgO catalysts for CO<sub>2</sub> reforming of methane: Activity and metal–Support interaction. *J. Mol. Catal. A Chem.* **2009**, *299*, 44–52. [[CrossRef](#)]
25. Zhang, Z.-F.; Liu, Z.-T.; Liu, Z.-W.; Lu, J. DMC Formation over Ce<sub>0.5</sub>Zr<sub>0.5</sub>O<sub>2</sub> Prepared by Complex-decomposition Method. *Catal. Lett.* **2008**, *129*, 428–436. [[CrossRef](#)]
26. Arena, F.; Licciardello, A.; Parmalian, A. The role of Ni<sup>2+</sup> diffusion on the reducibility of NiO/MgO system: A combined TPR-XPS study. *Catal. Lett.* **1990**, *6*, 139–1501. [[CrossRef](#)]
27. Liu, Y.J.; Qing, S.J.; Hou, X.N.; Qin, F.J.; Wang, X.; Gao, Z.X.; Xiang, H.W. Temperature dependence of Cu–Al spinel formation and its catalytic performance in methanol steam reforming. *Catal. Sci. Technol.* **2017**, *7*, 5069–5078. [[CrossRef](#)]
28. Taherian, Z.; Khataee, A.; Han, N.; Orooji, Y. Hydrogen production through methane reforming processes using promoted-Ni/mesoporous silica: A review. *J. Ind. Eng. Chem.* **2022**, *107*, 20–30. [[CrossRef](#)]
29. Chen, D.; Christensen, K.; Ochoafernandez, E.; Yu, Z.; Totdal, B.; Latorre, N.; Monzon, A.; Holmen, A. Synthesis of carbon nanofibers: Effects of Ni crystal size during methane decomposition. *J. Catal.* **2005**, *229*, 82–96. [[CrossRef](#)]
30. Park, K.S.; Cho, J.M.; Park, Y.M.; Kwon, J.H.; Yu, J.S.; Jeong, H.E.; Choung, J.W.; Bae, J.W. Enhanced thermal stability of Ni nanoparticles in ordered mesoporous supports for dry reforming of methane with CO<sub>2</sub>. *Catal. Today* **2022**, *388–389*, 224–230. [[CrossRef](#)]

31. Seo, J.-C.; Kim, H.; Lee, Y.-L.; Nam, S.; Roh, H.-S.; Lee, K.; Park, S.B. One-pot synthesis of full-featured mesoporous Ni/Al<sub>2</sub>O<sub>3</sub> catalysts via pyrolysis-assisted evaporation-induced self-assembly method for dry reforming of methane. *ACS Sustain. Chem. Eng.* **2021**, *9*, 894–904. [[CrossRef](#)]
32. Niu, J.; Wang, Y.; Liland, S.E.; Regli, S.K.; Yang, J.; Rout, K.R.; Luo, J.; Ronning, M.; Ran, J.; Chen, D. Unraveling enhanced activity, selectivity, and coke resistance of Pt-Ni bimetallic clusters in dry reforming. *ACS Catal.* **2021**, *11*, 2398–2411. [[CrossRef](#)]
33. Li, K.; Pei, C.; Li, X.; Chen, S.; Zhang, X.; Liu, R.; Gong, J. Dry reforming of methane over La<sub>2</sub>O<sub>2</sub>CO<sub>3</sub>-modified Ni/Al<sub>2</sub>O<sub>3</sub> catalysts with moderate metal support interaction. *Appl. Catal. B Environ.* **2020**, *264*, 118448. [[CrossRef](#)]
34. Ma, Q.; Han, Y.; Wei, Q.; Makpal, S.; Gao, X.; Zhang, J.; Zhao, T.-S. Stabilizing Ni on bimodal mesoporous-macroporous alumina with enhanced coke tolerance in dry reforming of methane to syngas. *J. CO<sub>2</sub> Util.* **2020**, *35*, 288–297. [[CrossRef](#)]

**Disclaimer/Publisher's Note:** The statements, opinions and data contained in all publications are solely those of the individual author(s) and contributor(s) and not of MDPI and/or the editor(s). MDPI and/or the editor(s) disclaim responsibility for any injury to people or property resulting from any ideas, methods, instructions or products referred to in the content.